Maccaferri, F., Rivalta, E., Passarelli, L., Jonsson, S. (2013): The stress shadow induced by the 1975-1984 Krafla rifting episode. - Journal of Geophysical Research, 118, 3, 1109-1121

DOI: 10.1002/jgrb.50134

JOURNAL OF GEOPHYSICAL RESEARCH: SOLID EARTH, VOL. 118, 1109–1121, doi:10.1002/jgrb.50134, 2013

The stress shadow induced by the 1975–1984 Krafla rifting episode

F. Maccaferri,[1,2] E. Rivalta,[1,2] L. Passarelli,[1,2] and S. Jónsson[3]

Received 7 October 2012; revised 25 January 2013; accepted 14 February 2013; published 28 March 2013.

[1] It has been posited that the 1975–1984 Krafla rifting episode in northern Iceland was responsible for a significant drop in the rate of earthquakes along the Húsavík-Flatey Fault (HFF), a transform fault that had previously been the source of several magnitude 6–7 earthquakes. This compelling case of the existence of a stress shadow has never been studied in detail, and the implications of such a stress shadow remain an open question. According to rate-state models, intense stress shadows cause tens of years of low seismicity rate followed by a faster recovery phase of rate increase. Here, we compare the long-term predictions from a Coulomb stress model of the rifting episode with seismological observations from the SIL catalog (1995–2011) in northern Iceland. In the analyzed time frame, we find that the rift-induced stress shadow coincides with the eastern half of the fault where the observed seismicity rates are found to be significantly lower than expected, given the historical earthquake activity there. We also find that the seismicity rates on the central part of the HFF increased significantly in the last 17 years, with the seismicity progressively recovering from west to east. Our observations confirm that rate-state theory successfully describes the long-term seismic rate variation during the reloading phase of a fault invested by a negative Coulomb stress. Coincident with this recovery, we find that the *b*-value of the frequency-magnitude distribution changed significantly over time. We conclude that the rift-induced stress shadow not only decreased the seismic rate on the eastern part of the HFF but also temporarily modified how the system releases seismic energy, with more large magnitude events in proportion to small ones. This behavior is currently being overturned, as rift-induced locking is now being compensated by tectonic forcing.

Citation: Maccaferri, F., E. Rivalta, L. Passarelli, and S. Jónsson (2013), The stress shadow induced by the 1975–1984 Krafla rifting episode, *J. Geophys. Res. Solid Earth*, *118*, 1109–1121, doi:10.1002/jgrb.50134.

1. Introduction

[2] Static and dynamic stress transfers have often proved useful in interpreting the main features of earthquake interactions [e.g., *Harris et al.*, 1995; *Stein et al.*, 1997; *Harris*, 1998; *Stein*, 1999; *Cocco et al.*, 2000]. In the last two decades, a large number of studies have used Coulomb failure stress changes to explain natural and anthropogenic earthquake triggering. Among all the processes related to stress transfer, stress shadows have, however, remained elusive, with some studies finding negative evidence [*Kilb*, 2003; *Felzer and Brodsky*, 2005] and others demonstrating their positive effects. *Shelly and Johnson* [2011] found tremor levels measured at 15–25 km depth on the San Andreas Fault (SAF) to be suppressed for about a month after the 2003 San Simeon earthquake. *Toda et al.* [2012] used a stress shadow to explain the systematic drop in seismicity caused by the M_w = 7.3 Landers earthquake (June 1992, California) in regions where the nearby M_w = 6.1 Joshua Tree quake (April 1992) had triggered aftershocks. *Sevilgen et al.* [2012] showed that the Sumatra 2004 *M*9.2 earthquake drastically reduced strike-slip events for 5 years, over a 750 km long segment of the Andaman rift-transform system by inducing a negative static Coulomb stress change on strike-slip receiver faults. More often, the concept of stress shadows has been used to relate present observations of low seismicity rates with the occurrence of past large earthquakes [*Reasenberg and Simpson*, 1992; *Simpson and Reasenberg*, 1994; *Jaumé and Sykes*, 1996; *Harris and Simpson*, 1996; *Lienkaemper et al.*, 1997; *Gahalaut et al.*, 2011]. For example, *Harris and Simpson* [1996] studied the correlation between the static stress change induced by the 1857 Fort Tejon earthquake (southern California) and all $M \geq 5.5$ earthquakes that occurred in the following years. They found the spatial correlation to disappear around 1907 and concluded that it took about 50 years for the tectonic loading to overcome the stress change caused by the Fort Tejon earthquake.

[3] Until now, authors have focused more on the predicted short-term seismicity rate changes than long-term

[1]GeoForschungsZentrum Potsdam, Potsdam, Germany.
[2]Institute of Geophysics, University of Hamburg, Hamburg, Germany.
[3]King Abdullah University of Science and Technology, Saudi Arabia.

Corresponding author: F. Maccaferri, GeoForschungsZentrum, Helmholtzstrasse 7, 14467 Potsdam, Germany. (francesco.maccaferri@gfz- potsdam.de)

2169-9313/13/10.1002/jgrb.50134

effects. For instance, *Belardinelli et al.* [2011] showed that the negative stressing rate during the subsidence in the Campi Flegrei caldera (Italy) following the 1982–1984 unrest damped the seismicity rate in the short term.

[4] The difficulty in identifying and demonstrating the existence of stress shadows has been attributed to two main limitations [*Hainzl et al.*, 2010; *Toda et al.*, 2012]: (i) Background seismicity rates are often too low to observe significant drops, and (ii) geometry and slip irregularities on fault planes produce local stress increases which may reduce or even mask the effect of stress shadows. Due to these limitations, most studies of stress shadows have primarily been qualitative.

[5] Here, we overcome these limitations by studying earthquake rate changes within the Tjörnes Fracture Zone (TFZ) in northern Iceland and the stress transferred there by a rifting episode that took place between 1975 and 1984 in the nearby Krafla volcanic system. The TFZ is seismically a very active area with hundreds to thousands of earthquakes recorded annually and has experienced several $M>6$ earthquakes during the last three centuries. Multiple dike intrusions during the Krafla rifting episode caused large stress changes in the area with the geodetic moment of the entire rifting episode estimated to be comparable to a $M_w=7$–8 earthquake [*Wright et al.*, 2012], thus producing a large stress change. When studying the stress transferred by the dike intrusions, the second limitation is overcome, because, in this case, the dislocation plane is lubricated by magma filling the dike. Consequently, the distribution of opening becomes much smoother than in a typical slip distribution in an earthquake, with the shear stresses becoming mostly relaxed on the dike surface.

[6] We quantitatively demonstrate that the stress changes associated with the rifting episode significantly reduced the Coulomb failure stress and inhibited the seismicity in the eastern section of the Húsavík-Flatey Fault (HFF), one of two main seismic lineations within the TFZ. Furthermore, we show that the rate-state theory [*Dieterich*, 1994] successfully describes how areas that experienced a negative Coulomb stress can gradually recover over a time scale of several decades to pre-rifting seismicity rates. We show that long-term effects have the advantage that they can be retrieved from the data even if the background rate is not well known.

[7] We also investigate the spatiotemporal variations of the parameters of the Gutenberg-Richter law, which have implications for the assessment of the seismic hazard in the populated eastern area of the HFF.

2. Geological Background and Earthquake Data

[8] The Tjörnes Fracture Zone is a ∼100 km transform offset in the Mid-Atlantic Ridge (MAR) in northern Iceland. It accommodates ∼2 cm/yr of transfer motion between the inland Northern Volcanic Zone (NVZ) and the offshore Kolbeinsey Ridge, a northward continuation of the MAR. The TFZ is not a single transform fault, but a zone consisting of at least two major transform structures, the Grímsey Oblique Rift (GOR) and the Húsavík-Flatey Fault (HFF) (see Figure 1). Modeling of continuous and campaign GPS velocities has shown that the GOR appears to accommodate 66% of the total transfer motion, while the remaining 34% seem to be focused on the HFF [*Metzger et al.*, 2011, 2012]. Several magnitude 6–7 earthquakes have occurred on both the GOR and the HFF in the past, as well as in the surrounding area, making the TFZ one of the two most seismically active areas in Iceland.

2.1. The Krafla Rifting Episode

[9] The Krafla volcanic system is one of several volcanic systems within the NVZ, which extends from the Vatnajökull glacier in the south to the northern shore of Iceland and the TFZ in the north (Figure 1). Each of the parallel and partially overlapping volcanic systems comprises a central volcano and an associated fissure swarm extending toward the north and south from the central volcano. The 1975–1984 rifting episode is the most recent in the NVZ, consisting of a series of about 20 dike intrusions [*Tryggvason*, 1984], which propagated laterally from the Krafla caldera (K in Figure 1) mostly to the north, although several propagated to the south as well. The first dike intrusion on 12 December 1975 was the largest of the entire episode and it propagated far north toward the GOR and triggered the 13 January 1976 magnitude 6.4 Kópasker earthquake [*Einarsson*, 1986; *Buck et al.*, 2006; *Passarelli et al.*, 2012]. Further diking events occurred during the following 10 years, resulting in a maximum surface extension of 8–9 m and an average opening of about 3.5 m [*Tryggvason*, 1984]. The rifting activated over 80 km of the fissure swarm system, extending 65 km to the north and 15 km to the south from the center of the Krafla caldera (Figure 2). The last dike event of the sequence was not described by *Tryggvason* [1984] but its opening was estimated to be about 1 m by *Árnadóttir et al.* [1998] and it extended ∼9 km to the north of the center of the caldera.

[10] The geodetic moment of the Krafla rifting episode has been compared to a $M_w=7$–8 earthquake [*Wright et al.*, 2012] and it certainly caused significant stress changes in the nearby fault systems within the TFZ. However, while the 1975 dike clearly increased the Coulomb stress on the GOR, triggering the 1976 Kópasker earthquake, the influence of stress of the rifting episode on the HFF remains less clear. This fault system is primarily a right-lateral strike-slip fault system with a N115°E strike along most of its length, but its easternmost and on-land portion has a slightly higher N125°E strike (Figure 1). It has been suggested that the Krafla rifting episode may have relaxed accumulated stresses along large parts of the HFF, opposite to what happened on the GOR, as a clear reduction in earthquake activity was noticed on the HFF following the start of the rifting episode (P. Einarsson, personal communication, 2012).

2.2. Historical and Instrumental Seismicity

[11] Figure 1 shows the estimated location and magnitude of the main earthquakes during the last 300 years, which include three magnitude 7 earthquakes and several events that have been estimated between magnitude 6 and 7. Among large earthquakes on the GOR are the magnitude 6.4 Kópasker earthquake in 1976, mentioned above, and a magnitude 7 earthquake in 1910. A large earthquake struck the HFF in 1755—it was estimated to be of size 7—and two magnitude 6.5 shocked the fault in 1872 with an interval of only 1 h. In addition to the events on the GOR and HFF,

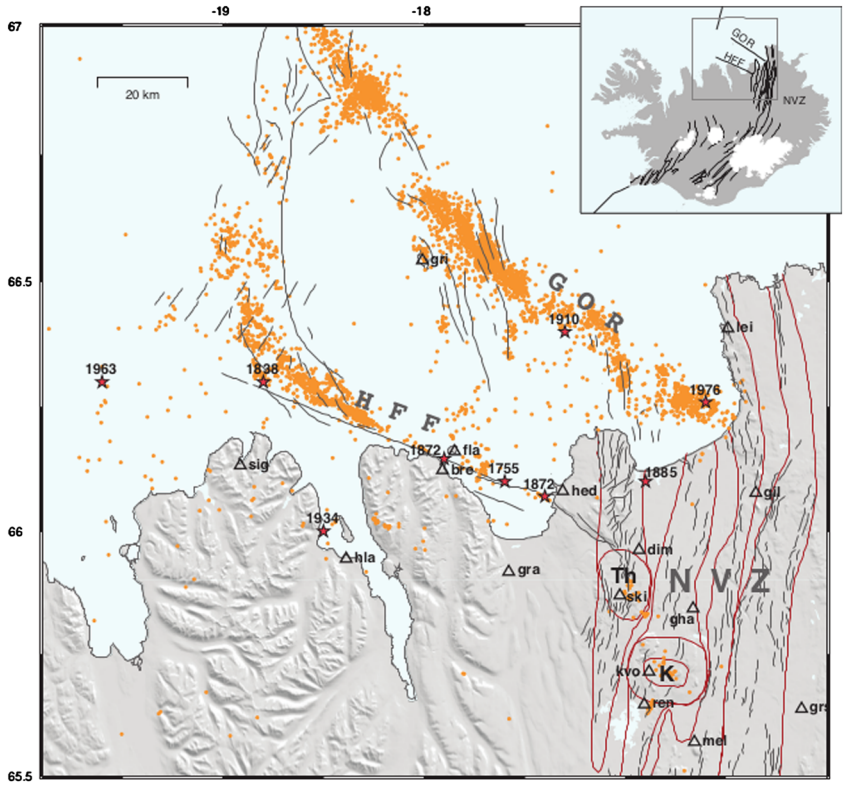

Figure 1. Earthquakes in the Tjörnes Fracture Zone (TFZ) between 1995 and 2011 (orange dots), clustering on the Grímsey Oblique Rift (GOR) and along the western part of the Húsavík-Flatey Fault (HFF). Red stars indicate the approximate locations of large (M>6) historical earthquakes. Secondary seismicity clusters mark the location of Theistareykir (Th) and Krafla (K) volcanoes within the Northern Volcanic Zone (NVZ). Thin black lines represent mapped fractures and faults, while red lines surround fissure swarms and central volcanoes. Black triangles mark the location of SIL network stations. The inset shows the location of the study area in North Iceland.

several large earthquakes have occurred to the southwest of the HFF, including a magnitude 7 in 1963 and a magnitude 6.3 in 1934 [*Stefansson et al.*, 2008].

[12] A network of modern seismological instruments (the SIL network) was installed in northern Iceland in 1994 and since then a coherent and high-quality seismic catalog has become available for the area. The network records over 2000 $M > 2$ earthquakes in the TFZ annually and the earthquake locations clearly highlight the two main lineaments in the TFZ, the GOR and HFF (Figure 1). In addition, significant diffused seismicity is found between the two lineaments and to the southwest of the HFF. Some of this diffused seismicity appears to follow north-to-south lineations and it has been suggested that these lineations may correspond to source regions of significant past earthquakes [*Stefansson et al.*, 2008].

[13] The eastern half of the HFF lacks seismicity, when compared to the western half, despite being the source of large earthquakes in 1755 and 1872. Prior to the start of the Krafla rifting episode, earthquakes along the eastern half of the HFF were not uncommon. However, following the start of the Krafla episode in 1975, this seismicity ceased and it has been suggested that this reduction in earthquake activity was caused by a stress shadow induced by the rifting episode [*Stefansson et al.*, 2008]. However, this idea has so far only been supported by evidence of the notable reduction in seismicity. It has not yet been backed up by quantitative stress-change calculations.

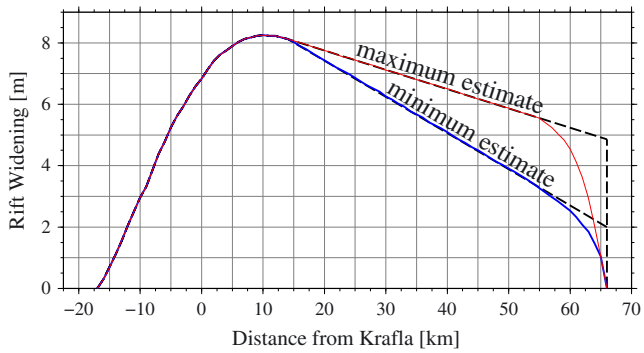

Figure 2. Estimated rift opening during the Krafla fissure swarm in relation to the distance to the north from the center of the caldera [from *Tryggvason*, 1984].

3. Stress Modeling and ΔCFS

[14] We model the stress perturbation due to the Krafla rifting episode (see Figure 2) as induced by a single and

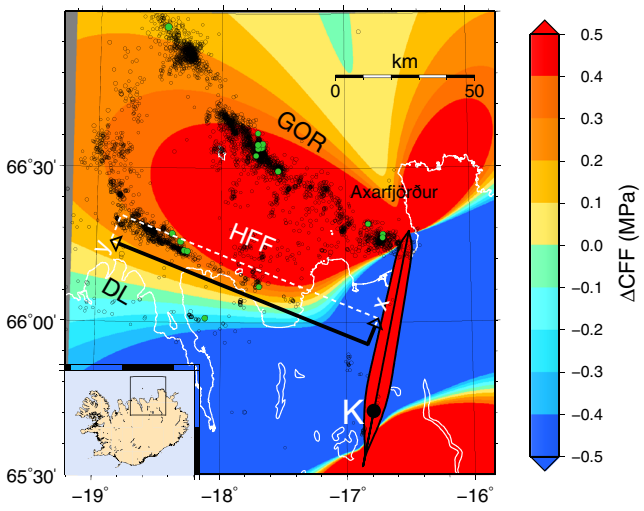

Figure 3. Map of the Coulomb failure stress changes induced by the Krafla rifting episode. Receiver faults are parallel to the average HFF strike (N68°W) with right-lateral mechanism. The stress source is a tensile crack striking N11°E with opening as Figure 2. The friction coefficient is set to 0.7. Black circles mark earthquakes from 1995 to 2011 above local magnitude M_l=2.0 (radius proportional to magnitude), while M_l>4 events are plotted in green. The white dashed rectangle with (x, y) axes highlights the study area along the HFF.

instantaneous intrusion. We neglect in our model the time dependence of the stress changes associated with individual diking events. A high-quality seismic catalog is only available from 1995. It would therefore be be impractical to relate temporarily varying stress changes occurring before 1984 to changes in seismicity rates observed more than a decade later. In addition, testing such a relation would significantly increase the number of parameters of the dike intrusion model. As geodetic data exist for only the surface rift extension during the rifting episode [*Tryggvason*, 1984], and no inversion results for the distributed dike opening at depth are available, we model the intrusion in two dimensions, with 88 elementary tensile dislocations in an infinite homogeneous elastic medium (the rigidity is 30 GPa and the Poisson's ratio is 0.25). We assume that the dike opened at depth as much as the total measured rift extension (Figure 2, "maximum estimate" curve). We consider this to be a conservative estimate of the cumulative opening of the magma intrusion that accumulated during the rifting episode as the surface rift extension should in general be somewhat smaller than the dike opening at depth if the dike does not reach the surface.

[15] We calculate variations in the Coulomb Failure Stress (ΔCFS) [*Harris*, 2003] on receiver faults that are oriented as the HFF (see Figure 3), using a friction coefficient, μ=0.8. Since the strike of the HFF varies along the fault [*Metzger et al.*, 2011], we also calculate the ΔCFS for receiver faults oriented ±10° with respect to the dominant strike of the HFF.

[16] The sources of error in the estimated Coulomb stress changes in our study are mainly due to (i) simplifying the rifting episode as a single event, (ii) neglecting a possible depth-dependent dike geometry, (iii) ignoring the opening due to the last (1984) diking event of the sequence, (iv) ignoring the deformation measured at Theistareykir volcano [see *Metzger et al.*, 2012], and (v) uncertainties in the physical parameters that are given as input for the model (friction, orientation). Varying the crustal rigidity or scaling the rift opening differently affects only the intensity of the stress changes but not the pattern, as the latter depends on the distribution of the opening along the rift rather than on the size of the opening or the rigidity of the crustal rocks. A similar argument applies to the plane-strain approximation chosen for the rift model: the other possible choice, the plane-stress approximation, would result in decreasing the value of the Coulomb stress by 6.25%.

[17] Poroelastic and viscoelastic effects have been shown to be significant in the Krafla rift system [*Foulger et al.*, 1992; *Pollitz and Sacks*, 1996; *Pedersen et al.*, 2009] and in Iceland in general [*Jónsson et al.*, 2003; *Jónsson*, 2008]. Poroelastic effects have time scales that are much shorter than the processes we are analyzing here [*Jónsson et al.*, 2003]. Most of the post-rifting deformation in time scales of a few tens of years has probably been caused by viscoelastic stress relaxation or continued intrusion in the lower crust or upper mantle; the effect in the upper crust could however be evaluated only by introducing a more complex model that would be difficult to constrain. We neglect here all these contributions to post-diking deformation, as their overall amplitude should be second order with respect to the direct stress changes caused by the rifting episode itself.

[18] Despite all the model uncertainties, we find excellent agreement between the region with negative ΔCFS and the eastern part of the HFF, where the 1995–2011 seismicity rate is lower than the historical one (see Figure 3 and compare with the historical earthquakes shown in Figure 1). The seismicity rate on the eastern part of the HFF is expected to be gradually increasing with time due to steady tectonic loading, as we will show in section 4.4. Areas invested with small negative ΔCFS will recover earlier with respect to areas with large negative ΔCFS.

4. Detailed Study of the HFF

[19] Models of stress shadows predict sudden drops in seismicity rates, followed by a slow recovery over time scales of several tens of years. As a good-quality catalog is available only from 1995, more than 10 years after the end of the rifting episode, we can only investigate a potential stress shadow effect on the TFZ by analyzing the seismicity rates relative to the recovery phase over a time interval of 17 years.

[20] We restrict our analysis to a rectangular region that is 100 km long and 10 km wide around the HFF (dashed white lines in Figure 3). The complete catalog for the HFF contains 16,912 events. From the plot of the cumulative seismicity (red curve, Figure 4a), several clusters can be identified. Some of them are due to mainshock-aftershock sequences; others are due to fluid intrusions, which are abundant on the TFZ [*Hensch et al.*, 2008]. Those clusters must be removed as they would dominate any small and slow seismicity rate changes.

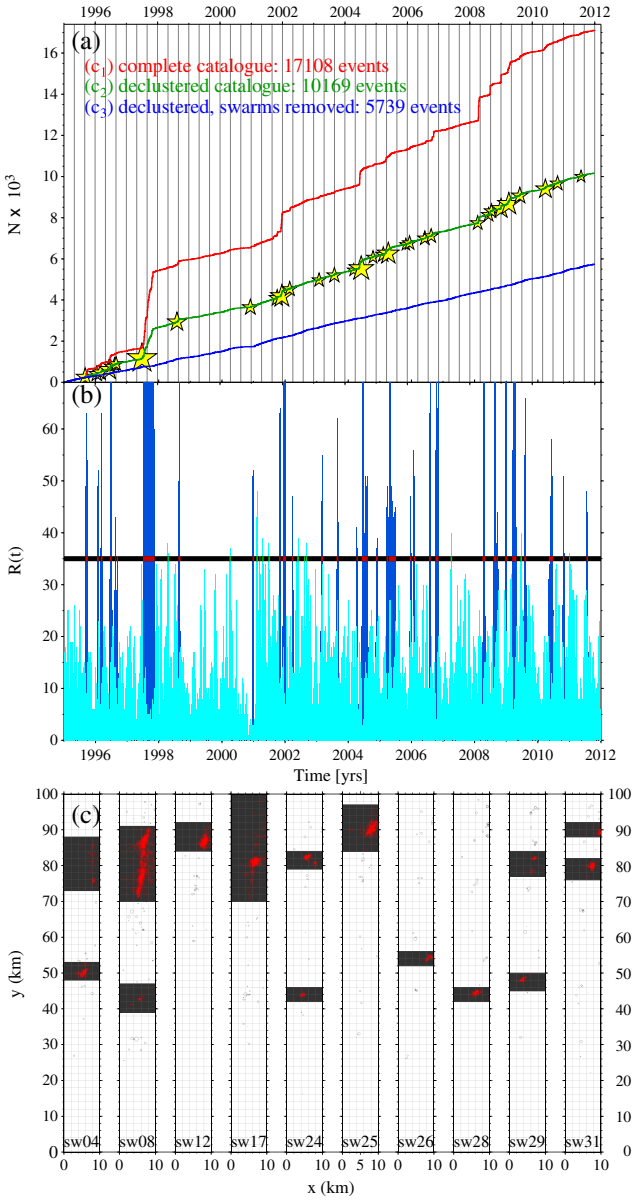

Figure 4. (a) In red, the cumulative number of earthquakes from the complete catalog (c_1) in the HHF area (white dashed rectangle in Figure 3). In green, the declustered catalog (c_2) obtained by applying the algorithm by *Reasenberg* [1985]. The stars indicate identified swarms that were removed from c_2, resulting in the blue curve (c_3). (b) A histogram showing the 2 weeks earthquake rate (14 day bins) with the black line showing twice the average 2 weeks event rate, above which fluid-induced swarms were suspected (dark blue bars). Red stripes on the black horizontal line indicate that a fluid-induced swarm was confirmed by finding tight space clustering. These swarms were removed resulting in the light blue histogram. Green stripes indicate that the high rate was associated to a cluster with fewer than 20 events, which were not removed. (c) Some examples of fluid-induced seismic swarms, which primarily were detected in two areas along the HFF: $40 \lesssim y \lesssim 55$ and $70 \lesssim y \lesssim 100$.

4.1. Declustering and "Deswarming"

[21] First, we remove the aftershock sequences that are caused by the stress induced by a larger earthquake nearby, rather than directly caused by the tectonic stress. We apply the declustering algorithm by *Reasenberg* [1985], which results in a declustered catalog containing 9985 events (Figure 4a, green line). Next, we apply a procedure to remove earthquakes caused by fluid intrusions. We proceed as follows: we calculate the mean earthquake rate for the whole period in the entire HFF rectangular box, obtaining an average of about 35 earthquakes per month. We then plot a histogram (Figure 4b) with the number of earthquakes recorded in time intervals of 2 weeks in each bar and identify the time frames when this number was larger than 35 (double the average rate), finding that this threshold is exceeded 44 times in the seismic catalog. We inspect the epicentral distribution during those time frames, and finally remove the earthquakes that cluster tightly in space, forming seismic clouds of 20 events or more (see some examples of removed swarms in Figure 4c).

[22] We identify a total of 37 spatially separated swarms, marked in Figure 4a with yellow stars, in the 44 inspected time frames. Note that some of the swarms took place within the same time frame but at different locations (see sw04, sw08, sw24, sw29, and sw31 in Figure 4c), so that the 37 swarms belong to 33 different time frames (named sequentially in time from sw01 to sw33). Clusters containing fewer than 20 events are not eliminated, so that the catalog is not entirely "deswarmed." We restrict the removal to this level to make the procedure the most objective and the least invasive as possible. The identified swarms are distributed approximately uniformly over the entire time period, which makes us confident that this operation did not introduce any significant artificial seismicity rate changes over long periods of time other than what was actually due to the tectonic loading.

[23] We divide the HFF area into five boxes (marked I–V) with homogeneous seismic features (see Figure 5a1). From the epicentral distribution in Figures 5a1 and 5a2 (catalogs c_1 and c_3, respectively), it can be seen that boxes III ($38<y<55$ km) and V ($68<y<100$ km) are affected by fluid-induced swarms, appearing as relatively scattered, slightly off-fault clusters, sometimes oriented at an angle of about 20°–40° with respect to the HFF. This orientation is compatible with the most compressive stress axis in the area, thus supporting the hypothesis of swarms induced by the intrusion of fluids. In boxes III and V, the seismic rates are significantly higher than in the other boxes and almost all the swarms we identified are located there. There are 11 swarms in box III and 25 in box V. Only one swarm was found in box IV ($55<y<68$ km) and no swarms in boxes I ($y<25$ km) and II ($25<y<38$ km). Box I is characterized by a nearly zero seismicity rate. Note that close to the boundary between boxes I and II, the HFF changes orientation (see thin red lines in Figures 5a1 and 5a2).

4.2. Coulomb Stress Changes on the HFF

[24] The main sources of error in Coulomb failure stress calculations are the orientation of the receiver fault and the source geometry and slip [*Hainzl et al.*, 2010b; *Woessner et al.*, 2012]. In this study, the geometrical uncertainty

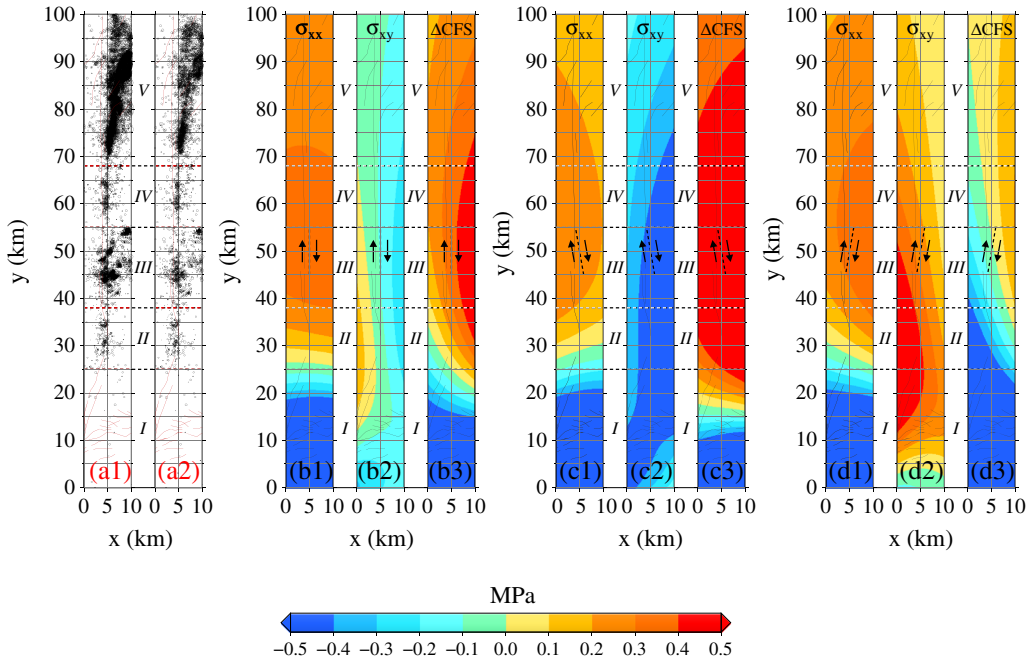

Figure 5. Seismicity and stress change calculations for the HFF. (a1 and a2) Earthquakes from the c_1 and c_3 catalogs, respectively. Thin red lines indicate mapped fractures and faults, note that the lines approximately parallel to x axis, for $0 < y < 20$ km, are mostly traces of diking events from Theistareykir rifting event (1867–1885) that partially intersect the HFF trace. (b1–d1) Normal and (b2–d2) shear components of the stress change (σ_{xx} and σ_{xz}, respectively) induced by the rift opening on receiver faults with strike and fault mechanism as indicated in each panel (dashed line with black arrows). (b3—d3) Resulting Coulomb stress changes. Thin black lines are mapped fractures on the HFF area.

translates into the relative orientation between the rift axis and the HFF, which itself is not exactly planar (Figure 5).

[25] We calculate the normal (Figures 5b1–5d1), shear (Figures 5b2–5d2), and Coulomb stress change (Figures 5b3–5d3) components on the HFF for three orientations of the receiver fault (average HFF strike and HFF strike ±10°, Figures 5b–5d). The calculated Coulomb stress changes switch signs from negative values in the east to positive values in the west. We find that this change from negative to positive ΔCFS moves significantly toward east or west with a minor change in the receiver fault strike. On one hand, this highlights the uncertainty in the Coulomb stress calculation that is related to the uncertainty of the relative angle between the rift and the fault. On the other hand, fault complexity may imply local deviations from the main strike of the HFF. Therefore, Coulomb stress changes should be projected on the individual patches on which earthquakes can potentially nucleate. In this way, ΔCFS values in the range of what is seen in Figures 5b–5d, all affect the seismicity of the HFF. In particular, Figure 5d shows that the stress shadow could extend out to box III, while the western part of the HFF (boxes IV and V) should not experience any reduction in ΔCFS even when a scattered orientation of the fault patches is considered.

[26] With the stress sign convention adopted here, negative shear stresses act in the same right-lateral direction as the tectonic loading. Our stress model of the Krafla rifting episode suggests that the shear stress loaded on the fault by the rifting contributed less to the Coulomb stress than the normal stress change. Although the portions of the fault that strike approximately in direction $y+10°$ (see Figure 5D2) were loaded with significant positive shear stresses ($\approx$ 0.3–0.5 MPa for $y<55$ km), the overall fault orientation is parallel to the y axis in Figure 5 and the shear stress is close to zero or even slightly negative ($<$0.1 MPa, Figure 5b2). On the other hand, according to our calculations, the rifting did compress the eastern portion of the fault (and decompress the western part) quite significantly. Indeed, for all fault orientations, there is strong compression for $y \lesssim 20$ km while a slight decompression is observed for $y \gtrsim 30$ km (see Figures 5b1–5d1). Moreover, the pressure change ($\sigma_{kk} = (\sigma_{xx}+\sigma_{yy}+\sigma_{zz})/3$) induced by the rifting episode compressed the entire HFF, with $|\sigma_{kk}|>0.5$ MPa for $y<60$ km and increasing toward east.

4.3. Seismicity Rate Changes on the HFF

[27] By analyzing the cumulative number of earthquakes in each box of the HFF (Figures 6a.Box I–6a.Box V), we can identify an increase in the slope of the cumulative number of earthquakes in boxes I–III, which corresponds to a relatively sharp increase in the seismicity rate. We can identify a knee point, t_k, separating two time intervals where the trend of the cumulative number of earthquakes is approximately linear. We estimate the knee point timing at the intersection between the two lines that approximate well the cumulative number of earthquakes before and after the clear rate increase. We find the knee occurs later in box I than in box II and later in box II than in box III or, in other words, we find that the transition in the seismicity rate migrates from NW to SE, i.e., toward the dike location. We estimate that the rate transition in box I took place in January 2005,

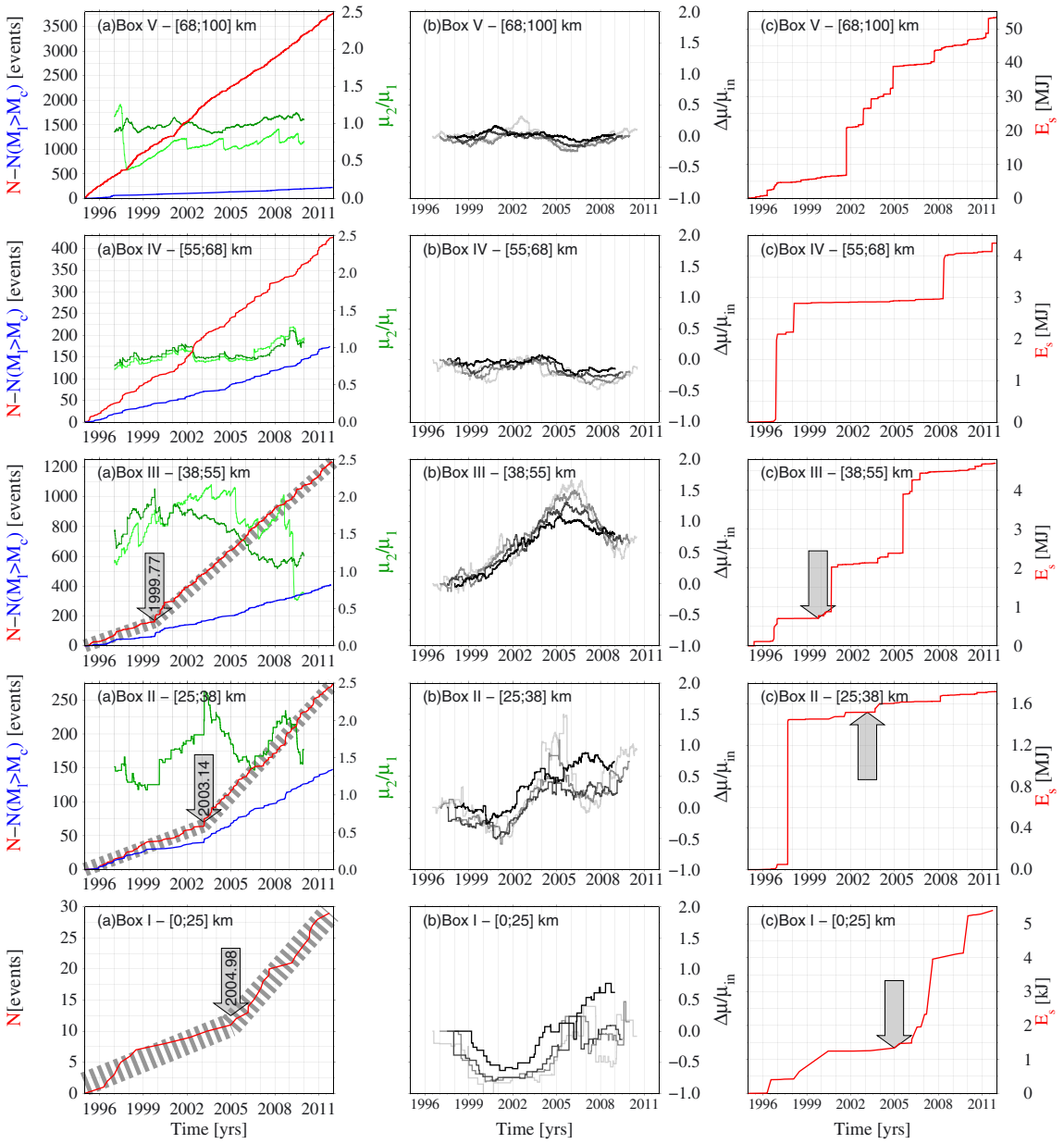

Figure 6. (a.Box I–a.Box V) In red, the cumulative number of earthquakes for the c_3 catalog. In blue, the cumulative number of earthquakes restricted to $M_l > M_c$ (local magnitude larger than the magnitude of completeness) for each box (see section 4.5 and Figure 9). The gray dashed lines in Figures 6a.Box I–6a.Box III highlight the change in the slope of the cumulative curves. The gray arrows indicate a knee point in the seismicity rate. In dark and light green, the ratio $[\mu_2/\mu_1](t)$ between the estimated background seismicity rate before and after time t (the c_3 catalog and the complete catalog c_1, respectively). (b.Box I–b.Box V) Relative maximum likelihood estimate of the seismicity rate, $(\mu - \mu_{in})/\mu_{in}$, calculated with the algorithm by *Hainzl et al.* [2006] on sliding windows of 3, 4, 5, and 6 years (from light to dark gray). The algorithm is applied to the complete catalog with swarms removed. (c.Box I–c.Box V) The cumulative energy released by the earthquakes $\log E_s \sim 2.0 \cdot M_l$ [from *Berckhemer and Lindenfeld*, 1986; *Bormann*, 2009, equation (3.86)].

although this estimate is based on only 30 earthquakes over a 17 year time frame. The estimate of the transition timing is more robust for boxes II and III, where many more earthquakes took place; there we find the knees in January 2003 and October 1999, respectively. At any rate, in order to avoid any artifact on the analysis of seismicity rates due to network improvement during the studied time frame, we calculate the knee points for boxes I–III also for $M > M_c$ (above the magnitude of completeness). The results do not change: we obtain the same time for the knee points in each cumulative (Figures 6a.Box I–6a.Box V). In boxes IV and V, the cumulative number of earthquakes does not show any seismicity rate change, in agreement with our rifting stress model (Figure 5) that predicts positive Coulomb stress

change (in the range of 0.1–0.5 MPa) for those boxes. Such a change in the Coulomb stress probably caused an increase in the seismic rate for a period shorter than the 11 years between the end of the rifting episode and the installation of the SIL network [*Passarelli et al.*, 2012], although this cannot be shown with the presented data set.

[28] We also check whether the data contradict the hypothesis of a constant seismic rate in each box across the entire time period. We calculate (green lines in Figures 6a.Box–6a.Box V) the ratio between the maximum likelihood estimation for a constant background rate [*Hainzl et al.*, 2006] after (μ_2) and before (μ_1) each time $t \in [1995, 2011]$. The function $\mu_r = \mu_2/\mu_1$ is larger than 1 when the estimated background rate for $[t, 2011]$ is larger than the estimated background rate for $[1995, t]$. In addition, μ_r is at maximum when the background rate changes the fastest. We show results obtained both with catalog c_3 (dark green curves) and with catalog c_1 (light green curves) for all boxes, except for box I where the small number of earthquakes prevents a solid maximum likelihood estimate of the background rate. For boxes II and III, the background-rate ratios of catalog c_3 show maxima that correspond with the timing of the knees found in the cumulative curves (Figure 6). We conclude that the seismicity in boxes I–III is compatible with a seismic rate increasing with time; the hypothesis of a steady seismic rate for the entire time interval [1995, 2011] hence has low likelihood. In box III, there is only one clear maximum in the curve, suggesting that there was only one significant increase in the seismic rate during the study period. In box II, on the other hand, we have a second relative maximum, in August 2008, suggesting a second significant increase in the seismicity rate. However, the estimate refers to a time relatively close to the margin of the analyzed time interval and is likely less robust. In boxes IV and V, $\mu_2/\mu_1 \simeq 1$ with just a weak maximum of $\mu_2/\mu_1 = 1.3$ close to the edge of the observed time frame in box IV. This confirms the hypothesis that in these boxes the seismicity rate was stationary during the study period.

[29] In boxes II and IV, where swarm occurrence is absent or small, the curves related to catalog c_3 and c_1 are superposed or are very similar. In boxes III and V, where multiple swarms occurred, the temporal behavior of the background-rate ratio for catalogs c_3 and c_1 differs more; in box III, we still observe a relative maximum in correspondence with the absolute maximum obtained with catalog c_3, but the absolute maximum related to catalog c_1 is in June 2003. Still, in box III, $\mu_2/\mu_1 > 1$, suggesting an increase of the seismicity rate, while in box V the fluctuations introduced by the presence of swarms appear to be randomly distributed and μ_2/μ_1 oscillates around (or close to) 1.

[30] The complete algorithm by *Hainzl et al.* [2006] is a declustering tool that eliminates all earthquakes with inter-event times not statistically consistent with a Poisson distribution (the expected distribution for a seismic catalog with constant background rate) from a seismic catalog. By working on sufficiently wide time windows to include a statistically relevant number of events, we can extrapolate information about temporal changes in the seismicity rate for each box of the HFF. We can also calculate the relative variation of the maximum likelihood estimate of the background rate $(\mu - \mu_{in})/\mu_{in}$ for all the boxes (Figure 6), where μ_{in} refers to the first time window while μ refers to the subsequent windows. The different curves (Figures 6b.Box I–6b.Box V), from light gray to black, refer to calculations on moving time windows of 3, 4, 5, and 6 years. While in box I the low number of earthquakes prevents statistically solid conclusions, we find for boxes II and III a clear trend of increasing seismicity rates. When shorter time windows are chosen, the seismicity rate shows large oscillations, but remains consistent with a positive secular trend of the seismicity rate. In boxes IV and V, the seismicity rate looks stable over all time-window lengths. We find that the increase in the seismicity rate is not mirrored in an increase in the rate of energy released by the earthquakes (with the possible exception of box I), calculated according to the equation: $\log E_s \sim 2.0 \cdot M_l$ [from *Berckhemer and Lindenfeld*, 1986; *Bormann*, 2009, equation (3.86)] (see Figures 6c.Box I–6c.Box V). The relation between the seismic rate and the rate of seismic energy will be discussed in section 4.5, where we study the frequency-magnitude distribution of the earthquakes in each box.

4.4. Modeling Changes in the Seismicity Rate

[31] Changes in the seismicity rate are often modeled by using the rate-state formulation, which links relative variations in the seismicity rate with respect to the background seismicity to changes in the Coulomb stress. In the HFF, however, different stress contributions are active in the same time frame: beside the tectonic stressing, the stress caused by the largest earthquakes and the stress induced by fluids ascending in the crust also generate seismicity. In the rate-state formulation, these contributions are entangled in a nonlinear way and it is not possible to separate them. Hence, this model cannot be applied to our declustered and deswarmed catalogs. Another difficulty is that since the rifting episode occurred before the SIL became operational, we cannot estimate a background seismicity rate. However, it is useful to discuss the observations in terms of the rate-state model because it allows a physical understanding of the seismicity changes. With this purpose, we restrict the application to boxes I, II, and IV, which are free of swarms and of larger magnitude events.

[32] According to the rate-state formulation of *Dieterich* [1994], a decrease (or an increase, not studied here) in Coulomb stress on a population of faults is associated with a sudden drop (or increase) in the seismicity rate equal to

$$R = r \exp\left(\frac{\Delta \mathrm{CFS}}{A\sigma}\right), \tag{1}$$

where r is the background rate, A is a constitutive parameter, and σ is the effective normal stress. The time-dependent seismicity rate during the recovery phase (see Figure 7) is [*Hainzl et al.*, 2010]

$$R = r \frac{1}{1 + \left[\exp\left(-\frac{\Delta \mathrm{CFS}}{A\sigma}\right) - 1\right] \exp\left(-\frac{\dot{\tau} t}{A\sigma}\right)}, \tag{2}$$

where $\dot{\tau}$ is the stressing rate (for the HFF $\dot{\tau} = 5 \cdot 10^{-3}$ MPa/yr). Positive ΔCFS values are linked to relatively short bursts of seismicity, with the magnitude of the Coulomb stress affecting mostly the intensity of the bursts rather than their duration (see Figure 7 and section A1 in the Appendix, equation (A3)). Conversely, a negative ΔCFS depresses seismicity rates for time scales that depend strongly on the

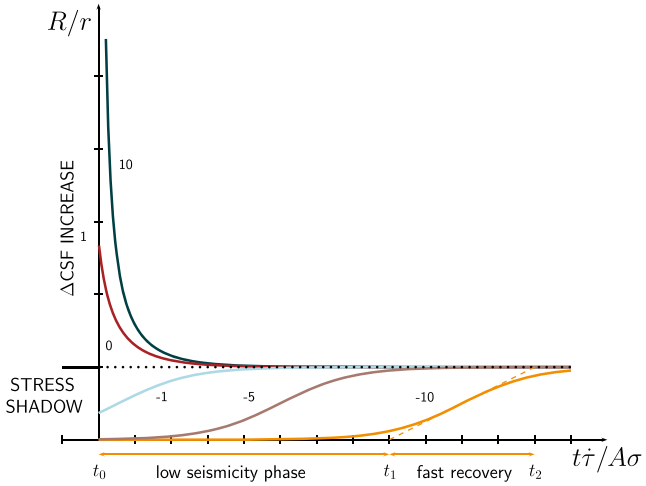

Figure 7. Temporal evolution of the predicted seismic rate for different ratios $\Delta CFS/A\sigma$ (labeled in black). The seismicity rate at $t=0$ jumps to $\exp(\Delta CFS/A\sigma)$. For $\Delta CFS>0$, a peak is followed by an exponential decay to pre-stress rates (black dotted line). The time scale of the decay is $\approx A\sigma/\dot{\tau}$ (approximately weeks) and does not depend on the intensity of ΔCFS. For negative Coulomb stresses, an abatement is followed by a recovery to pre-stressing rates which does depend on ΔCFS: the time scale is $\approx -\Delta CFS/\dot{\tau}$, which for reasonable values of the parameters may be tens of years, several orders of magnitude larger than for positive ΔCFS. Hence, opposite ΔCFS values may be linked to very different time scales of recovery.

intensity of the stress shadow (see Figure 7, and section A1, equation (A4)). This occurs because a longer duration of steady tectonic stress loading is needed to compensate for the larger stress drop and for R to return to r (Appendix A1, equation (A4)).

[33] The functional behavior of equation (2) (see also Figures 7 and 8) provides insight into how to interpret the spatiotemporal variations observed in the seismicity data. After an application of a stress shadow at $t = t_0 = 0$, the seismicity rate drops to R_{low} and remains approximately constant until $t = t_1 = -(\Delta CFS + 2A\sigma)/\dot{\tau}$, which, for example, translates into 16 years for $\Delta CFS = -1$ bar $= -0.1$ MPa, $A\sigma = 0.01$ MPa, and $\dot{\tau} = 5 \cdot 10^{-3}$ MPa yr^{-1} (or 18 years if $A\sigma = 0.005$ MPa). This implies that, for the parameter values above, we should observe the end of the low seismicity phase about 16–32 years (or 18–36 years) after the event where $\Delta CFS \in [-0.2, -0.1]$ MPa. This is consistent with the results shown in Figure 5, as the rifting episode occurred during the 11–20 years before the beginning of the seismicity time series and 27–36 years before the end date of our analysis (December 2011). Thus, we should see the end of the low seismicity phase in boxes that were subjected to $\Delta CFS \in [-0.2, -0.1]$ MPa. Only a small portion of the HFF appears to have experienced a reduction in the ΔCFS in this range (Figure 5) but this location corresponds to where we observe the easternmost burst of seismicity on the HFF (see box II in Figures 5a1 and 5a2).

[34] After the low seismicity phase, a fast recovery begins. This recovery is roughly linear, with slope $\dot{\tau}/4A\sigma$, and it lasts for a time, $\Delta t_{rec} \approx 4A\sigma/\dot{\tau}$, until $t=t_2=(-\Delta CFS + 2A\sigma)/\dot{\tau}$ (see Appendix A and *Harris and Simpson* [2003, p.1218]). From the cumulative curves in Figure 6, it is difficult to estimate how long the recovery phase lasts, but it seems to be about 4 years at most. This would imply, for $\dot{\tau} = 5 \cdot 10^{-3}$ MPa/yr, that $A\sigma = 5 \cdot 10^{-3}$ MPa or less. This value is somewhat low but not unreasonable according to published estimates for other regions.

4.5. Earthquake Statistics on the HFF

[35] We conclude by analyzing the statistics of earthquake occurrences on the HFF with the purpose of identifying if the marked changes in seismic rate are mirrored in changes in the *b*-values. We estimate the parameters of the Guntenberg-Richter (GR) distribution (magnitude of completeness, M_c, and slope, b) for boxes II to V, but exclude box I due to the lack of earthquakes. We estimate the GR statistics for the time frames before and after the knee points identified in the cumulative seismicity (Figure 6). Since the seismicity produced by fluid intrusions is not distributed according to the GR [e.g., *Wiemer and Wyss*, 2002], we use the "deswarmed" catalog, where we retain the aftershocks but remove the fluid-induced swarms already identified in section 4.1. To derive the GR statistics, we use the *b*-stability method first proposed by *Cao and Gao* [2002] and modified by *Woessner and Wiemer* [2005] for sample sets with more than 50 events. We then estimate the uncertainties for the *b*-values and M_c as one standard deviation of 10,000 bootstrap simulations of the seismic catalog.

[36] The *b*-value varies substantially with time and space along the HFF (Figure 9). In boxes II and III, the *b*-values inferred for earthquakes occurring before the knee point are very low (0.62 ± 0.06 and 0.73 ± 0.07). Note that the value before the knee point for Box II was inferred from only 66 earthquakes and should be regarded with caution. Also, the

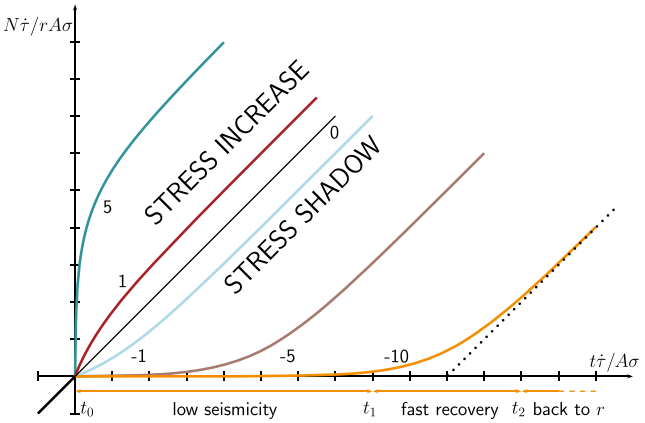

Figure 8. Temporal evolution of the predicted cumulative seismicity for different ratios, $\Delta CFS/A\sigma$ (labeled in black). The cumulative seismicity increases linearly with slope r for $t<0$. For positive ΔCFS, there is a sharp increase followed by a deceleration toward the background slope (black solid line). For $\Delta CFS<0$, the cumulative seismicity curve becomes flat and then recovers to the background slope (black dotted line). Note that for negative stress changes, the recovery time to the background rate is much longer than for positive stress changes.

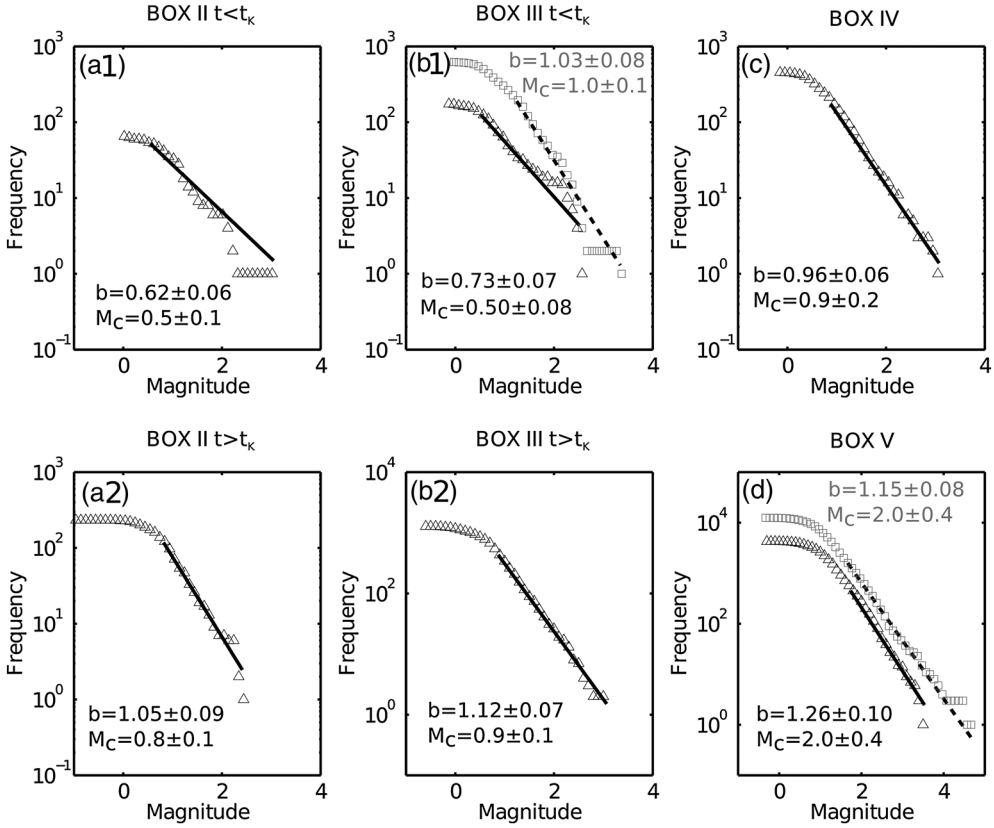

Figure 9. Cumulative frequency-magnitude distribution of earthquakes (black triangles) from the deswarmed catalog and best fit for the Gutenberg-Richter (GR) (black lines, estimated with the *b*-stability method [*Cao and Gao*, 2002; *Woessner and Wiemer*, 2005]). The magnitude of completeness, M_c, and the *b*-value for the best fit are reported in each inset. Gray squares, dashed lines, and results in gray refer to the complete catalog (c_1); the results for the two catalogs (deswarmed and complete) are mostly indistinguishable and hence reported only in Figures 9B1 and 9D, where the difference is significant. (a1, a2, b1, and b2) For boxes II and III, we calculate separately the best fit for the data before and after the knee points, t_k. (c and d) For boxes IV and V, we consider the whole time series.

estimated uncertainties are probably somewhat too small, as *b*-value estimates depend on the statistical method used (see Figure 10a.Box II, where a different method was used to estimate *b*-value variations in time). These *b*-values, more typical of compressive regimes [*Schorlemmer et al.*, 2005], are compatible with intense clamping of these portions of the HFF. After the knee point, the seismic regime seems to have changed: the *b*-values for boxes II and III are ∼1.05 and 1.12, consistent with faults confined at lower stress [*Schorlemmer et al.*, 2005]. These results are consistent with fault locking due to the stress shadow induced by the rifting (more strain could accumulate on the fault due to an increase in the effective friction caused by compressive stresses, resulting in the strengthening of the population of asperities), followed by a successful recovery to the pre-rifting stress regime. We statistically verify whether two separate regimes, with different *b*-values, are needed to describe the statistics for boxes II and III before and after the knee point. For this, we use the Utsu test [*Utsu*, 1999], based on the Akaike information criterion (AIC). In both cases, we obtain $\Delta AIC \gg 2$, which confirms that two different *b*-values, rather than a single one for the full time series, describe the GR statistic significantly better for boxes II and III. The significant change in time of the *b*-values for boxes II and III reveals an evolution of the magnitude-frequency distribution of the earthquakes for these portions of the HFF fault. In boxes II and III, for $t < t_k$, the *b*-values indicate the higher frequency of the larger magnitude events. This explains why the rate of energy release is not correlated with the changes in the seismicity rate before and after t_k (Figures 6c.Box I–6c.Box III). Although the seismic rates in boxes II and III were significantly lower before the knee points, the *b*-values were so low that large magnitude events (M>6) were actually more likely to occur than later on, after the knee point. This conclusion is based on extrapolating the GR statistics to magnitudes considerably larger than the range used to estimate the parameters, which is a questionable operation.

[37] The *b*-values for box III (for $t > t_k$) and for box V ($b = 1.26$) are consistent with the presence of fluids (see Figure 5c), influencing the earthquake statistics by lowering friction and limiting stress accumulation. From the GR analysis of the complete catalog c_1 (in gray in Figure 9), we find the estimates for M_c and *b* to match almost exactly with the estimates based on the deswarmed catalog, except for box III (before the knee point, where we find $b = 1.03$) and for box V ($b = 1.16$). However for box III, the Utsu test still indicates that the GR statistics for before and after the knee point is better described with two different *b*-values.

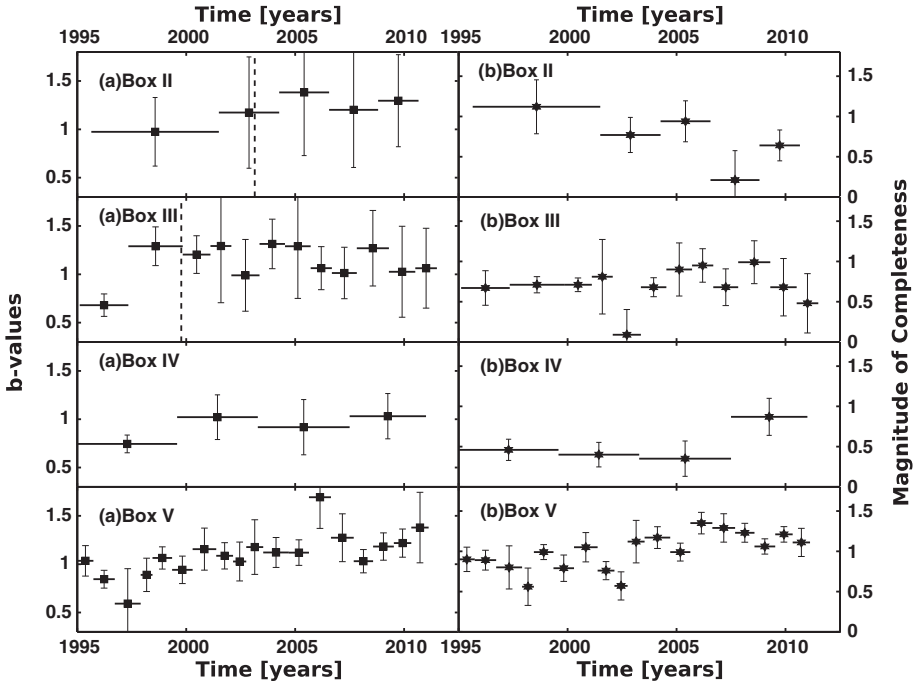

Figure 10. Evolution with time of the (a.Box II–a.Box II V) *b*-value and (b.Box II–b.Box V) M_c for boxes II–V, respectively. The *b*-values and M_c are calculated using the maximum curvature method [*Woessner and Wiemer*, 2005], as the *b*-stability method [*Cao and Gao*, 2002; *Woessner and Wiemer*, 2005] used in Figure 9 does not converge for all subsets of events. For each box, individual values for *b* and M_c are calculated using a subset of data points: 50 for box II (Figures 10a.Box II and 10b.Box II, respectively), 100 for boxes III and IV (Figures 10a.Box III, 10a.Box IV, 10b.Box III, and 10b.Box IV) and 200 for box V (Figures 10a.Box V and 10b.Box V). The time interval covered varies (generally, it decreases with time, mirroring the increase in time of the seismicity rate) and is indicated by a horizontal segment over each symbol.

[38] The SIL network was installed in several stages. By 21 January 1994, the five key stations for locations in the TFZ were operating (sig, gri, gra, gil, and lei). On 1 February 1995, station hla was installed. On 30 August 1996 hrn was installed, whereas the hed, fla, and bre stations were installed only on 9 November 2000. These three additional stations may have increased the location accuracy and the magnitude of completeness. To further explore the robustness of our results, we study the time evolution of the *b*-values and M_c for the individual boxes. We calculate the *b*-value and M_c for every *N* earthquakes in the time series, with *N*=50, 100, 100, and 200 for boxes II–V, respectively, resulting in varying the time intervals (Figure 10). The increase in the seismic rate is reflected in the shortening of the time intervals containing *N* data points, which is especially visible in boxes II and III. The dashed lines mark the knee point timing and divide the regimes with lower rates and low *b*-values from regimes with higher rates and high *b*-values in boxes II and III. We do not find that the network improvements in 2000 led to a decrease in M_c, except possibly for box II. We therefore believe that our results are not affected significantly by the installation of additional stations (see Figures 10b.Box II–10b.Box V).

[39] The high-quality monitoring network that was installed in 1995 in the TFZ and NVZ has been crucial for carrying out this study. This network will also be critical for assessing changes in seismic hazard deriving from the evolution of the regional and local stress field and volcanic activity. When designing monitoring activities aimed at studying important events (e.g., earthquakes and rifting episodes), the need for a complete earthquake catalog that includes the event itself as well as the years before and after it should be considered. For example, a similar catalog for the rifting episode in the Manda-Harraro segment (Mid Ethiopian Rift) cannot be compiled due to temporal discontinuities and inhomogeneities in the monitoring, hampering similar studies on the physics and statistics of the interaction of magmatism with faulting.

5. Conclusions

[40] In summary,

[41] 1. We find that negative Coulomb stress changes due to the 1975–1984 Krafla rifting episode provide a satisfying explanation for the mismatch between historical earthquake activity and seismic data from the last 17 years in the Tjörnes Fracture Zone.

[42] 2. We find that the seismicity rate on the eastern part of the Húsavík-Flatey Fault continues to increase activating the fault progressively closer to the Krafla fissure swarm. This supports the hypothesis that the stress shadow due to the rifting event is still affecting the seismic rate of the HFF.

[43] 3. More intense negative Coulomb stresses, induced on the easternmost part of the HFF, will affect the seismicity for a long time, possibly for tens of years.

[44] 4. Despite the intense stress shadow, which usually drastically reduces seismicity rates to very low levels, here enough earthquakes are left that an estimate of the GR parameters is possible. We find that the *b*-value has increased significantly over time along the eastern portion of the HFF. This is consistent with unclamping in the fault during the time interval we study and could be related to the stress shadow we identified. The observed *b*-value variations suggest that stress changes might also modify the release of seismic energy, while a frictional model alone is not able to make a prediction about the magnitudes of induced seismic events.

[45] 5. The space-time evolution of the seismicity rates, of the *b*-values, and of the moment release seem entangled in a complicated way. Thus, it seems difficult to use this information in a prospective way to assess, for example, whether large magnitude events have been delayed by the stress shadow.

[46] 6. We infer that magmatic activity in the NVZ, specifically large diking events or rifting episodes, has the potential to change the state of stress suddenly and significantly in the TFZ, to trigger large earthquakes or abate seismicity for tens of years. The current state of stress, reflected in the low seismicity rates of the eastern portion of the HFF and to the south of it, may be overturned by, for example, a large magmatic event in the nearby NVZ (including the Theistareykir, Krafla, or Askja volcanoes), as this could transfer intense positive Coulomb stresses to the portion of HFF currently locked and accumulating tectonic strain. Hence, close monitoring of the NVZ is important for time-varying hazard assessment in the TFZ.

Appendix A: Rate-State Equations

[47] The time-dependent seismicity rate after a step change in Coulomb stress is [*Hainzl et al.*, 2010]

$$R = r\frac{1}{1+\left[\exp\left(-\frac{\Delta CFS}{A\sigma}\right)-1\right]\exp\left(-\frac{\dot{\tau}t}{A\sigma}\right)}. \quad (A1)$$

The number, N, of earthquakes expected in a time interval, Δt, can be calculated from

$$\frac{\dot{\tau}N}{rA\sigma} = \ln\left[1+\left(\exp\left(\frac{\dot{\tau}\Delta t}{A\sigma}\right)-1\right)\exp\left(\frac{\Delta CFS}{A\sigma}\right)\right]. \quad (A2)$$

A1. Behavior of the Seismic Rate for Different ΔCFS Values

[48] The behavior of equation (A1) differs depending on the sign and intensity of the ΔCFS:

[49] 1. $\Delta CFS \gg A\sigma$ (significantly positive stress changes): The term $\exp\left(-\frac{\Delta CFS}{A\sigma}\right)$ in equation (A1) becomes very small and negligible with respect to 1. The formula can thus be approximated as follows:

$$R = r\frac{1}{1-\exp\left(-\frac{\dot{\tau}t}{A\sigma}\right)}. \quad (A3)$$

[50] 2. $\Delta CFS \ll -A\sigma$ (significantly negative stress changes): The term $\exp\left(-\frac{\Delta CFS}{A\sigma}\right)$ in equation (A1) becomes very large, much larger than 1, so that the formula can be approximated as follows:

$$R = r\frac{1}{1+\exp\left(\frac{-\Delta CFS-\dot{\tau}t}{A\sigma}\right)}. \quad (A4)$$

[51] 3. $-A\sigma \ll \Delta CFS \ll A\sigma$ (very small negative and positive stress changes): Given that $A\sigma \approx 10^{-2}$ MPa and given that ΔCFS patterns close to faults usually show quick spatial gradients from negative to positive values, areas subjected by this range of ΔCFS are small (at least in the near-field, while in the far-field they become not only very large and interesting, but also very sensitive to concurrent stress changes by other phenomena).

A2. The Seismicity Rate During Recovery From a Stress Shadow

[52] Assuming that $\Delta CFS \ll -A\sigma$ and that the approximation from equation (A4) holds, we observe that we can further approximate the curve with a plateau $R = r\exp(\Delta CFS/A\sigma)$ followed by a linear increase to $R = r$ (see Figure 7). In order to do that, we calculate the derivative at the inflection point during the recovery phase.

[53] First derivative:

$$\frac{d(R/r)}{dt} = \frac{\dot{\tau}/A\sigma\,\exp(-\frac{\Delta CFS+\dot{\tau}t}{A\sigma})}{\left[1+\exp(-\frac{\Delta CFS+\dot{\tau}t}{A\sigma})\right]^2}; \quad (A5)$$

Second derivative:

$$\frac{d^2(R/r)}{dt^2} = \frac{(\dot{\tau}/A\sigma)^2\exp\left(-\frac{\Delta CFS+\dot{\tau}t}{A\sigma}\right)}{\left[1+\exp\left(-\frac{\Delta CFS+\dot{\tau}t}{A\sigma}\right)\right]^2}\left[\frac{\exp(-\frac{\Delta CFS+\dot{\tau}t}{A\sigma})-1}{\exp(-\frac{\Delta CFS+\dot{\tau}t}{A\sigma})+1}\right]. \quad (A6)$$

The second derivative is equal to 0 for exp()=1, so for $t=t_c=-\Delta CFS/\dot{\tau}$. The value of the seismic rate at $t=t_c$ is $R_c/r=0.5$, and the slope of the rate is $d(R/r)/dt_{R=R_c} = \dot{\tau}/(4A\sigma)$.

[54] Approximating the seismicity rate for $t \ll t_c$ with $R/r = \exp(\Delta CFS/\dot{\tau})$, and the recovery phase as linearly increasing with time with a rate $\dot{\tau}/(4A\sigma)$, we find that the recovery starts at $t = -(\Delta CFS + 2A\sigma)/\dot{\tau}$ and proceeds until $t = (-\Delta CFS + 2A\sigma)/\dot{\tau}$, for a total approximate duration of $\Delta t_{rec} = 4A\sigma/\dot{\tau}$.

[55] Finally, the recovery phase for $\Delta CFS << -A\sigma \approx -0.01$ can be approximated by

$$\frac{R}{r} = \begin{cases} \exp\left(\frac{\Delta CFS}{A\sigma}\right) & \text{if } t \le \frac{-\Delta CFS-2A\sigma}{\dot{\tau}}, \\ \frac{\dot{\tau}t+\Delta CFS}{4A\sigma}+\frac{1}{2} & \text{if } \frac{-\Delta CFS-2A\sigma}{\dot{\tau}} < t < \frac{-\Delta CFS+2A\sigma}{\dot{\tau}}, \\ 1 & \text{if } t \ge \frac{-\Delta CFS+2A\sigma}{\dot{\tau}}. \end{cases} \quad (A7)$$

[56] **Acknowledgments.** We thank Martin Hensch, Sebastian Heimann, and Doreen Kasper for their help with the seismicity analysis. We also thank Maria Elina Belardinelli and an anonymous reviewer for their comments that improved this paper. We thank the Icelandic Meteorological Office (IMO) for providing the seismic data. This work was funded by the ERC starting grant project CCMP-POMPEI, grant 240583.

References

Árnadóttir, T., F. Sigmundsson, and P. T. Delaney (1998), Sources of crustal deformation associated with the Krafla Iceland eruption of September 1984, *Geophys. Res. Lett.*, *25*(7), 1043–1046.

Belardinelli, M. E., A. Bizzarri, G. Berrino, and G. P. Ricciardi (2011), A model for seismicity rates observed during the 1982–1984 unrest at Campi Flegrei caldera (Italy), *Earth planet. Sci. Lett.*, *302*, 287–298, doi: 10.1016/j.epsl.2010.12.015.

Berckhemer, H., and M. Lindenfeld (1986), Determination of source energy from broadband seismograms, *Geol. Jahrbuch*, *E*(35), 79–83.

Bormann, P. (ed.) (2009), *New Manual of Seismological Observatory Practice (NMSOP-1), IASPEI*, GFZ German Research Centre for Geosciences, Potsdam.

Buck, R., P. Einarsson, and B. Brandsdóttir (2006), Tectonic stress and magma chamber size as controls on dike propagation: Constraints from the 1975–1984 Krafla rifting episode, *J. Geophys. Res.*, *111*, B12,404, doi:10.1029/2005JB003879.

Cao, A., and S. Gao (2002), Temporal variation of seismic b-values beneath northeastern Japan island arc, *Geophys. Res. Lett.*, *29*(9), 48–1, doi: 10.1029/2001GL013775.

Cocco, M., C. Nostro, and G. Ekström (2000), Static stress changes and fault interaction during the 1997 Umbria-Marche earthquake sequence, *Journal of Seismology*, *4*(4), 501–516.

Dieterich, J. (1994), A constitutive law for rate of earthquake production and its application to earthquake clustering, *J. Geophys. Res.*, *99*(B2), 2601–2618.

Einarsson, P. (1986), Seismicity along the eastern margin of the North American Plate, *The Geology of North America*, *1000*, 99–116.

Felzer, K. R., and E. E. Brodsky (2005), Testing the stress shadow hypothesis, *J. Geophys. Res.*, *110*(B5), B05S09, doi:10.1029/2004JB003277.

Foulger, G., C. Jahn, G. Seeber, P. Einarsson, B. Julian, and K. Heki (1992), Post-rifting stress relaxation at the divergent plate boundary in Northeast Iceland, *Nat. Geosci.*, *358*, 488–490.

Gahalaut, V., S. Rajput, and B. Kundu (2011), Low seismicity in the Bhutan Himalaya and the stress shadow of the 1897 Shillong Plateau earthquake, *Phys. Earth Planet. Inter.*, *186*(3–4), 97–102, doi: 10.1016/j.pepi.2011.04.009.

Hainzl, S., F. Scherbaum, and C. Beauval (2006), Estimating background activity based on interevent-time distribution, *Bull. Seism. Soc. Am.*, *96*(1), 313–320, doi:10.1785/0120050053.

Hainzl, S., S. Steacy, and D. Marsan (2010), Seismicity models based on Coulomb stress calculations, *Community Online Resource for Statistical Seismicity Analysis*, doi:10.5078/corssa-32035809.

Hainzl, S., G. Zöller, and R. Wang (2010b), Impact of the receiver fault distribution on aftershock activity, *J. Geophys. Res.*, *115*, B05,315, 12, doi:10.1029/2008JB006224.

Harris, R. A. (1998), Introduction to special section: Stress triggers, stress shadows, and implications for seismic hazard, *J. Geophys. Res.*, *103* (B10), 24,347–24,358.

Harris, R. A., and R. Simpson (1996), In the shadow of 1857—The effect of the Great Ft. Tejon Earthquake on subsequent earthquakes in Southern California, *Geophys. Res. Lett.*, *23*(3), 229–232.

Harris, R. A. (2003), Stress triggers, stress shadows, and seismic hazard, in *International Handbook of Earthquake and Engineering Seismology,* Part B, vol. 81B, chap. 73, edited by W. H. K. Lee et al., Academic Press, San Diego, Calif.

Harris, R. A., R. W. Simpson, and P. A. Reasenberg (1995), Influence of static stress changes on earthquake locations in southern California, *Nat. Geosci.*, *375*, 221–224, doi:10.1038/375221a0.

Hensch, M., C. Riedel, J. Reinhardt, T. Dahm, and The-NICE-People (2008), Hypocenter migration of fluid-induced earthquake swarms in the Tjörnes Fracture Zone (North Iceland), *Tectonophysics*, *447*(1–4), 80–94, doi:10.1016/j.tecto.2006.07.015.

Jaumé, S. C., and L. R. Sykes (1996), Evolution of moderate seismicity in the San Francisco Bay region, 1850 to 1993: Seismicity changes related to the occurrence of large and great earthquakes, *J. Geophys. Res.*, *101*(B1), 765–789.

Jónsson, S. (2008), Importance of post-seismic viscous relaxation in southern Iceland, *Nat. Geosci.*, *1*, 136–139, doi:10.1038/ngeo105.

Jónsson, S., P. Segall, R. Pedersen, and G. Björnsson (2003), Post-earthquake ground movements correlated to pore-pressure transients, *Nat. Geosci.*, *424*, 179–183, doi:10.1038/nature01776.

Kilb, D. (2003), A strong correlation between induced peak dynamic Coulomb stress change from the 1992 M7. 3 Landers, California, earthquake and the hypocenter of the 1999 M7. 1 Hector Mine, California, earthquake, *J. Geophys. Res.*, *108*(B1), 2012.

Lienkaemper, J. J., J. S. Galehouse, and R. W. Simpson (1997), Creep response of the hayward fault to stress changes caused by the Loma Prieta earthquake, *Science*, *276*, 2014–2016, doi: 10.1126/science.276.5321.2014.

Metzger, S., S. Jónsson, and H. Geirsson (2011), Locking depth and slip-rate of the Húsavík, Flatey Fault, North Iceland, derived from continuous GPS data 2006-2010, *Geophys. J. Int.*, *187*, 564–576, doi:10.1111/j.1365-46X.2011.05176.x.

Metzger, S., S. Jónsson, G. Danielsen, S. Hreinsdóttir, F. Jouanne, T. Villemin, and D. Giardini (2012), Present kinematics of the Tjörnes Fracture Zone, North Iceland, from campaign and continuous GPS measurements, *Geophys. J. Int.*, *192* (2), 441–455, doi:10.1093/gji/ggs032.

Passarelli, L., F. Maccaferri, E. Rivalta, T. Dahm, and E. Abebe Boku (2012), A probabilistic approach for the classification of earthquakes as "triggered" or "not triggered", *J. Seismol., 17*, 165–187, doi: 10.1007/s10950-012-9289-4.

Pedersen, R., F. Sigmundsson, and T. Masterlark (2009), Rheologic controls on inter-rifting deformation of the Northern Volcanic Zone, Iceland, *Earth Planet. Sc. Lett.*, *281*, 14–26, doi:10.1016/j.epsl.2009.02.003.

Pollitz, F. F., and I. S. Sacks (1996), Viscosity structure beneath northeast Iceland, *J. Geophys. Res.*, *101*, 17,771–17,793.

Reasenberg, P. (1985), Second-order moment of central California seismicity, 1969–1982, *J. Geophys. Res.*, *90*(B7), 5479–5495.

Reasenberg, P. A., and R. W. Simpson (1992), Response of regional seismicity to the static stress change produced by the Loma Prieta earthquake, *Science*, *255*, 1687–1690.

Sevilgen, V., R. S. Stein, and F. F. Pollitz (2012), Stress imparted by the great 2004 Sumatra earthquake shut down transforms and activated rifts up to 400 km away in the Andaman Sea, *PNAS*, *109*(38), 15152–15156, doi:10.1073/pnas.1208799109.

Schorlemmer, D., S. Wiemer, and M. Wyss (2005), Variations in earthquake-size distribution across different stress regimes, *Nat. Geosci.*, *437*(7058), 539–542, doi:10.1038/nature04094.

Shelly, D., and K. Johnson (2011), Tremor reveals stress shadowing, deep postseismic creep, and depth-dependent slip recurrence on the lower-crustal San Andreas fault near Parkfield, *Geophys. Res. Lett.*, *38*, L13,312, doi:10.1029/2011GL047863.

Simpson, R. W., and P. A. Reasenberg (1994), Earthquake-induced static-stress changes on central California faults, in *The Loma Prieta, California, Earthquake of October 17, 1989–Tectonic Processes and Models*, edited by R. W. Simpson, no. 1550-F in U.S. Geol. Surv. Prof. Pap., U.S. Gov. Printing Office, F55–F89, Washington, D. C.

Stefansson, R., G. Gudmundsson, and P. Halldorsson (2008), Tjörnes fracture zone. New and old seismic evidences for the link between the North Iceland rift zone and the Mid-Atlantic ridge, *Tectonophysics*, *447*, 117–126, doi:10.1016/j.tecto.2006.09.019.

Stein, R. S. (1999), The role of stress transfer in earthquake occurrence, *Nat. Geosci.*, *402*(6762), 605–609.

Stein, R. S., A. A. Barka, and J. H. Dieterich (1997), Progressive failure on the North Anatolian fault since 1939 by earthquake stress triggering, *Geophys. J. Int.*, *128*(3), 594–604.

Toda, S., R. S. Stein, G. C. Beroza, and D. Marsan (2012), Aftershocks halted by static stress shadows, *Nat. Geosci.*, *5* (6), 410–413, doi: 10.1038/ngeo1465.

Tryggvason, E. (1984), Widening of the Krafla fissure swarm during the 1975–1981 volcano-tectonic episode, *Bull. Volcanol.*, *47*(1), 47–69.

Utsu, T. (1999), Representation and analysis of the earthquake size distribution: A historical review and some new approaches, *Pure Appl. Geophys.*, *155*(2-4), 509–535.

Wiemer, S., and M. Wyss (2002), Mapping spatial variability of the frequency-magnitude distribution of earthquakes, *Adv. Geophys.*, *45*, 259–302.

Woessner, J., and S. Wiemer (2005), Assessing the quality of earthquake catalogues: Estimating the magnitude of completeness and its uncertainty, *Bull. Seism. Soc. Am.*, *95* (2), 684–698, doi: 10.1785/0120040007.

Woessner, J., S. Jónsson, H. Sudhaus, and C. Baumann (2012), Reliability of Coulomb stress changes inferred from correlated uncertainties of finite-fault source models, *J. Geophys. Res.*, *117*, B07,303, doi: 10.1029/2011JB009121.

Wright, T. J., et al. (2012), Geophysical constraints on the dynamics of spreading centres from rifting episodes on land, *Nat. Geosci.*, *5*(4), 242–250, doi:10.1038/ngeo1428.